

## Two-dimensional stress analysis of functionally graded solids using the MLPG method with radial basis functions

D.F. Gilhooley<sup>a,c</sup>, J.R. Xiao<sup>e</sup>, R.C. Batra<sup>d</sup>, M.A. McCarthy<sup>a,b,c,\*</sup>, J.W. Gillespie Jr.<sup>e,f,g</sup>

<sup>a</sup> Composites Research Centre, University of Limerick, Ireland

<sup>b</sup> Materials and Surface Science Institute, University of Limerick, Ireland

<sup>c</sup> Department of Mechanical and Aeronautical Engineering, University of Limerick, Ireland

<sup>d</sup> Department of Engineering Science and Mechanics, Virginia Polytechnic Institute and State University, Blacksburg, VA 24061, USA

<sup>e</sup> Center for Composite Materials, University of Delaware, Newark, DE 19716, USA

<sup>f</sup> Department of Materials Science and Engineering, University of Delaware, Newark, DE 19716, USA

<sup>g</sup> Department of Civil and Structural Engineering, University of Delaware, Newark, DE 19716, USA

Received 19 March 2007; accepted 5 May 2007

Available online 22 June 2007

### Abstract

The meshless local Petrov–Galerkin (MLPG) method is used for analysing two-dimensional (2D) static and dynamic deformations of functionally graded materials (FGMs) with material response modelled as either linear elastic or as linear viscoelastic. The multiquadric radial basis function (RBF) is employed to approximate the trial solution. Results are computed with two different choices of test functions, namely a fourth-order spline weight function, and a Heaviside step function, each having a compact support. No background mesh is used to numerically evaluate integrals appearing in the weak formulation of the problem, thus the method is truly meshless. A benefit of using RBFs is that they possess the Kronecker delta property; thus it is easy to satisfy essential boundary conditions. For five problems, the computed results are found to match well with those either from their analytical solutions or numerical solutions of other researchers who employed different algorithms. For a dynamic problem, the Laplace-transform technique is utilised. The numerical examples illustrate that displacements and stress distributions in a structure made of an FGM differ considerably from those at the corresponding points in the same structure made of a homogeneous material. Thus, the inhomogeneity in material properties can be exploited to optimise stress distribution, minimise deflection and reduce the maximum stress.

© 2007 Elsevier B.V. All rights reserved.

**Keywords:** Functionally graded material; MLPG method; Radial basis functions; Static and dynamic problems

### 1. Introduction

Functionally graded materials (FGMs) are composites with material properties varying continuously in one or more directions according to a predetermined profile. These materials have been introduced to exploit the ideal performance of their constituents, e.g., heat/corrosion resistance of ceramics on one side, and mechanical strength and toughness of metals on the other side of a plate like

body. Ideally, FGMs have no interfaces among constituents giving them an advantage over conventional laminated composites because delamination failure mode is eliminated. FGMs also permit tailoring of material composition to optimise desired characteristics such as minimising deflections or stresses, or maximising the first frequency of free vibration. As a result, FGMs have potential applications in a wide variety of engineering components or systems, which include armour plating, heat engine parts and human implants.

The variation of material properties in an FGM is usually achieved by continuously varying volume fractions of their constituents. FGMs with material properties varying

\* Corresponding author. Tel.: +353 61 202222; fax: +353 61 202944.  
E-mail address: [michael.mccarthy@ul.ie](mailto:michael.mccarthy@ul.ie) (M.A. McCarthy).

only in one direction can be manufactured either by high-speed centrifugal casting [1,2] or by depositing ceramic layers on a metallic substrate [3,4]. An FGM with properties changing in the plane of a sheet can be produced by ultraviolet irradiation to alter the chemical composition [5]. A directed oxidation technique has also been employed [6,7] to deposit a ceramic layer on the outside surfaces of a structure. FG fibre-reinforced composites can be fabricated by varying the volume fraction of fibres and/or their orientation in the preform prior to infusing resin into it. Commercially developed FGMs are available for use as structural elements in different applications. Here, we study two-dimensional (2D) deformations of FG solids modelled as either linear elastic or linear viscoelastic.

Approximate solutions of realistic engineering problems are usually obtained numerically. Meshless methods such as the element-free Galerkin (EFG) method [8], the Reproducing Kernel particle method (RKPM) [9], hp-clouds [10], the partition of unity method (PUM) [11], the meshless local Petrov–Galerkin (MLPG) method [12,13], the smoothed particle hydrodynamics (SPH) [14], the corrected smoothed particle hydrodynamics (CSPH) [15], and the modified smoothed particle hydrodynamics (MSPH) [16] have attracted considerable attention recently. As the name implies, in the MLPG method a weak formulation of the problem is derived on a sub-domain of the region occupied by the body. These sub-regions may overlap and their union while contained in the entire domain may differ from it by a small amount. Depending upon the choice of test function, six MLPG formulations have been labelled as MLPG1 through MLPG6 in [13]. The basis functions for the trial solution and/or the test function can be generated by the moving least squares (MLS) approximation [8], the PUM using Shepard functions [11], the RKPM [9] or the MSPH [16]; however, these are generally rational functions and lack the Kronecker delta property. Thus, special techniques such as the use of penalty parameters or Lagrange multipliers, or the modification of the resulting system of linear algebraic equations are needed to satisfy essential boundary conditions. Recently, radial basis functions (RBFs) [17] have been employed to solve partial differential equations [18–20] and to approximate the trial solution in meshless methods [21–24]. RBFs possess the Kronecker delta property which facilitates satisfying essential boundary conditions. Furthermore, when RBFs are used in the weak formulation of a problem defined on a local domain (such as that in an MLPG method [24–26]) rather than over a global domain, dense matrices appearing in the global interpolation are avoided. The modified multiquadrics (MQ) and the thin plate spline (TPS) radial basis functions have been successfully employed to approximate a trial solution in the MLPG formulation [24,25] for solving 2D elastic problems. The MQ and TPS RBFs have also been employed for the analysis of homogeneous [26] and laminated plates [27].

Meshless methods have been used to analyse deformations of structures comprised of FGMs. Ching and Yen [28,29] used the MLPG method, with test function equal

to the weight function used to generate the MLS basis function (MLPG1), to study static and transient thermoelastic 2D deformations of FG elastic solids. Sladek et al. [30] set the test function equal to a Heaviside step function (MLPG5) to study static and dynamic 2D deformations of FG solids. They also used a modified fundamental solution as the test function in the MLPG method [31,32] to analyse heat conduction in FGMs. Rao and Rahman [33] used the EFG method to study fracture of FGMs, and Goupee and Vel [34] have combined the EFG with a genetic algorithm to optimise the composition of FGMs. Qian et al. [35–38] combined the MLPG1 method with the higher-order shear and normal deformable plate theory (HOSNDPT) of Batra and Vidoli [39] to study static and dynamic deformations of FG elastic and thermoelastic plates, transient heat conduction in an FG plate, and in-plane distribution of constituents to optimise the fundamental frequency of vibration of a beam. All of the above-mentioned researchers who used the MLPG method have employed the MLS basis functions to approximate the trial solution. Special techniques used to enforce essential boundary conditions increased the computational cost. We have employed the RBFs for the trial solution in an MLPG method for analysing FG plates [40]. RBFs have also been used in a collocation method by Ferreira et al. for studying static deformations [41] and free vibrations [42] of FG plates. Dai et al. [43] have employed RBFs in the radial point interpolation method to analyse static and dynamic deformation of piezoelectric FG plates.

Analytical solutions of static and dynamic problems for simply supported thermoelastic FG rectangular plates have been given by Vel and Batra [44,45], for a clamped elliptic plate by Cheng and Batra [46], and for a pressurised hollow cylinder and a rotating disk by Horgan and Chan [47]; the latter are summarised in chapter 10 of Batra's book [48].

Here, 2D static and dynamic deformation FG linear elastic or linear viscoelastic solids is analysed with two MLPG methods – one uses a fourth-order spline function of compact support as the test function (MLPG1) and the other employs a Heaviside step function (MLPG5) as the test function. The MQ RBFs are used to approximate the trial solution. These methods are applied to find numerical solutions of five problems, and computed results are compared with either their analytical solutions or numerical solutions reported by other researchers. Contributions of this work include comparing the performance of two numerical schemes for a class of elastostatic and elastodynamic problems for inhomogeneous bodies. It is found that for static problems the MLPG5 method requires less CPU resources than the MLPG1 formulation, and for the same number and locations of nodes the two formulations give results that compare very well with those obtained analytically.

## 2. Interpolation using radial basis functions

Consider a continuous function  $u(\mathbf{x})$  defined on a 2D domain  $\Omega$  having a set of suitably located nodes in it. An

interpolation of  $u(\mathbf{x})$  in the neighbourhood of a point  $\mathbf{x}_Q$  using RBFs and polynomial basis is written as

$$u(\mathbf{x}) = \sum_{i=1}^n g_i(\mathbf{x})a_i(\mathbf{x}_Q) + \sum_{j=1}^m p_j(\mathbf{x})b_j(\mathbf{x}_Q) = G^T a + P^T b \quad (1)$$

with the constraint

$$\sum_{i=1}^n p_j(x_i, y_i)a_i = 0, \quad j = 1, 2, \dots, m. \quad (2)$$

Here,  $g_i(\mathbf{x})$  is a radial basis function associated with node  $i$ ,  $p_j(\mathbf{x})$  is a monomial in the space coordinates  $\mathbf{x}^T = [x, y]$ ,  $n$  is the number of nodes in the neighbourhood of  $\mathbf{x}_Q$ ,  $m$  is the number of monomial basis functions (usually  $m < n$ ), and  $a_i(\mathbf{x}_Q)$  and  $b_j(\mathbf{x}_Q)$  are coefficients for  $g_i(\mathbf{x})$  and  $p_j(\mathbf{x})$ , respectively, that vary with the point  $\mathbf{x}_Q$ . The vectors  $a$ ,  $b$ ,  $G$  and  $P$  in Eq. (1) are defined as

$$a = [a_1, a_2, a_3, \dots, a_n]^T, \quad (3a)$$

$$b = [b_1, b_2, b_3, \dots, b_m]^T, \quad (3b)$$

$$G^T = [g_1(\mathbf{x}), g_2(\mathbf{x}), g_3(\mathbf{x}), \dots, g_n(\mathbf{x})]^T, \quad (3c)$$

$$P^T = [p_1(\mathbf{x}), p_2(\mathbf{x}), p_3(\mathbf{x}), \dots, p_m(\mathbf{x})]^T. \quad (3d)$$

The RBF is a function of the Euclidean distance  $r$  between points  $\mathbf{x}$  and  $\mathbf{x}_i$ . That is

$$g_i(\mathbf{x}) = g_i(r_i), \quad (4a)$$

$$r_i = [(x - x_i)^2 + (y - y_i)^2]^{1/2}. \quad (4b)$$

Eq. (4a) implies that  $g_i(\mathbf{x})$  is function of a scalar variable. The polynomial term in Eq. (1) is added to guarantee the non-singularity of the RBF interpolation and a 2D problem has the following set of complete monomials:

$$P^T = [1, x, y, x^2, xy, y^2, \dots]. \quad (5)$$

Requiring that the function  $u(\mathbf{x})$  given by Eq. (1) equals its value at  $n$  nodes in the vicinity of the point  $\mathbf{x}_Q$ , we get the following set of simultaneous linear algebraic equations for the coefficients  $a_i$  and  $b_j$ :

$$u(x_k, y_k) = \sum_{i=1}^n a_i g_i(x_k, y_k) + \sum_{j=1}^m b_j p_j(x_k, y_k), \quad (6)$$

$$k = 1, 2, 3, \dots, n.$$

Eqs. (6) and (2) can be expressed in matrix form as follows:

$$\begin{bmatrix} G_0 & P_0 \\ P_0^T & 0 \end{bmatrix} \begin{Bmatrix} a \\ b \end{Bmatrix} = \begin{Bmatrix} u^e \\ 0 \end{Bmatrix}, \quad (7)$$

where

$$u^e = [u_1, u_2, u_3, \dots, u_n]^T, \quad (8)$$

$$G_0 = \begin{bmatrix} g_1(x_1, y_1) & g_2(x_1, y_1) & \cdots & g_n(x_1, y_1) \\ g_1(x_2, y_2) & g_2(x_2, y_2) & \cdots & g_n(x_2, y_2) \\ \vdots & \vdots & \vdots & \vdots \\ g_1(x_n, y_n) & g_2(x_n, y_n) & \cdots & g_n(x_n, y_n) \end{bmatrix}_{n \times n}, \quad (9)$$

$$P_0 = \begin{bmatrix} p_1(x_1, y_1) & p_2(x_1, y_1) & \cdots & p_m(x_1, y_1) \\ p_1(x_2, y_2) & p_2(x_2, y_2) & \cdots & p_m(x_2, y_2) \\ \vdots & \vdots & \vdots & \vdots \\ p_1(x_n, y_n) & p_2(x_n, y_n) & \cdots & p_m(x_n, y_n) \end{bmatrix}_{n \times m}. \quad (10)$$

The solution of Eq. (7) is

$$\begin{Bmatrix} a \\ b \end{Bmatrix} = A^{-1} \begin{Bmatrix} u^e \\ 0 \end{Bmatrix}, \quad (11)$$

where

$$A = \begin{bmatrix} G_0 & P_0 \\ P_0^T & 0 \end{bmatrix} \quad (12)$$

and conditions (2) ensure that the matrix  $A$  is non-singular and hence invertible. Thus Eq. (1) becomes

$$u(\mathbf{x}) = [G^T(\mathbf{x})P^T(\mathbf{x})]A^{-1} \begin{Bmatrix} u^e \\ 0 \end{Bmatrix} = \Phi(\mathbf{x})u^e, \quad (13)$$

where

$$\Phi(\mathbf{x}) = [\phi_1(\mathbf{x}), \phi_2(\mathbf{x}), \phi_3(\mathbf{x}), \dots, \phi_k(\mathbf{x}), \dots, \phi_n(\mathbf{x})] \quad (14)$$

are the shape functions in which

$$\phi_k(\mathbf{x}) = \sum_{i=1}^n g_i(\mathbf{x})\bar{A}_{i,k} + \sum_{j=1}^m p_j(\mathbf{x})\bar{A}_{n+j,k}. \quad (15)$$

Here,  $\bar{A}_{i,k}$  is the  $(i, k)$  element of the matrix  $A^{-1}$ . The derivatives of  $\phi_k(\mathbf{x})$  can be obtained as follows:

$$\frac{\partial \phi_k}{\partial x} = \sum_{i=1}^n \frac{\partial g_i}{\partial x} \bar{A}_{i,k} + \sum_{j=1}^m \frac{\partial p_j}{\partial x} \bar{A}_{n+j,k}, \quad (16a)$$

$$\frac{\partial \phi_k}{\partial y} = \sum_{i=1}^n \frac{\partial g_i}{\partial y} \bar{A}_{i,k} + \sum_{j=1}^m \frac{\partial p_j}{\partial y} \bar{A}_{n+j,k}. \quad (16b)$$

The extended MQ function [49] is defined by

$$g_i(x, y) = (r_i^2 + c^2)^\beta, \quad (17)$$

where  $\beta$  and  $c$  are shape parameters. For  $\beta = 0.5$  and  $-0.5$ , Eq. (17) gives, respectively, the original Hardy's MQ [17] and the inverse MQ functions.

### 3. MLPG formulation

#### 3.1. Local weak form for static 2D deformations of a linear elastic body

Consider the following 2D problem defined on the domain  $\Omega$  with boundary  $\Gamma$ :

$$\sigma_{ij,j} + b_i = 0 \quad \text{in } \Omega, \quad (18)$$

$$t_i = \sigma_{ij}n_j = \bar{t}_i \quad \text{on } \Gamma_t, \quad (19a)$$

$$u_i = \bar{u}_i \quad \text{on } \Gamma_u. \quad (19b)$$

Here,  $\sigma_{ij}$  is the stress tensor,  $u_i$  the displacement field,  $b_i$  the body force vector,  $(\cdot)_{,j}$  denotes  $\partial(\cdot)/\partial x_j$ ,  $n_j$  is the unit outward normal to the boundary  $\Gamma$ , and  $\bar{u}_i$  and  $\bar{t}_i$  denote, respectively, the prescribed displacements and tractions. Bound-

ary conditions (19a) and (19b) are called natural and essential, respectively.

A weak form of Eq. (18) over a subdomain  $\Omega_s$  of domain  $\Omega$  and bounded by  $\Gamma_s$ , obtained by using the weighted residual method is

$$\int_{\Omega_s} v_i(\sigma_{ij,j} + b_i) d\Omega = 0, \quad (20)$$

where  $v_i$  is a test function. Neither Lagrange multipliers nor penalty parameters appear in Eq. (20) because essential boundary conditions can be imposed directly by using the interpolation Eq. (1) as is done in the finite element method. The application of the divergence theorem in Eq. (20) gives

$$\begin{aligned} & \int_{\Omega_s} \sigma_{ij} v_{i,j} d\Omega - \int_{\Gamma_{st}} t_i v_i d\Gamma - \int_{\Gamma_{su}} t_i v_i d\Gamma \\ & = \int_{\Gamma_{st}} \bar{t}_i v_i d\Gamma + \int_{\Omega_s} b_i v_i d\Omega, \end{aligned} \quad (21)$$

where  $\Gamma_{st}$  is the intersection of  $\Gamma_t$  and  $\Gamma_s$ , and  $\Gamma_{su}$  is the intersection of  $\Gamma_u$  and  $\Gamma_s$ .

We choose the test function  $v_i(x)$  such that it is positive in  $\Omega_s$  and vanishes outside  $\Omega_s$ . Even though the shape of  $\Omega_s$  can be arbitrary, in practice, it is taken to be either a circle or a rectangle; we take it to be a circle.

### 3.1.1. Test function

Atluri and Shen [13] have proposed six different choices for test functions and labelled the corresponding formulations as MLPG1 through MLPG6. Here we take the test function to be either a fourth-order spline function or a Heaviside step function. The corresponding two MLPG formulations are called MLPG1 and MLPG5, respectively. Qian and Batra [50] have compared the performances of MLPG1 and MLPG5 for static and dynamic deformations of a plate made of a homogeneous and isotropic material. The fourth-order spline function of compact support  $r_s$  is defined by

$$\psi_j = W(\mathbf{x} - \mathbf{x}_j) = \begin{cases} 1 - 6\left(\frac{d_j}{r_s}\right)^2 + 8\left(\frac{d_j}{r_s}\right)^3 - 3\left(\frac{d_j}{r_s}\right)^4, & 0 \leq d_j \leq r_s, \\ 0, & d_j \geq r_s \end{cases} \quad (22)$$

and the Heaviside step function by

$$\psi_j = W(\mathbf{x} - \mathbf{x}_j) = \begin{cases} 1, & 0 \leq d_j \leq r_s, \\ 0, & d_j \geq r_s. \end{cases} \quad (23)$$

Here,  $d_j = |\mathbf{x} - \mathbf{x}_j|$ . The circular subdomain  $\Omega_s$  has radius  $r_s$  and centre at the node located at  $x_i$ , hereafter also called node  $i$  or  $x_i$ ; thus the support of  $W$  equals the size of the subdomain.

### 3.1.2. Discretisation and numerical implementation

The displacement  $u$  in the neighbourhood  $\Omega_s$  of node  $i$  is approximated by Eq. (1) or equivalently by Eq. (13). Referring the reader to [24] for details, for a linear elastic mate-

rial one can deduce the following system of linear algebraic equations from Eq. (21).

$$\sum_{j=1}^n K_{ij} u^j = f_i. \quad (24)$$

For the MLPG1 method

$$\begin{aligned} K_{ij} &= \int_{\Omega_s} [B_i][D][B_j] d\Omega - \int_{\Gamma_{st}} [\Psi_i][N][D][B_j] d\Gamma \\ &\quad - \int_{\Gamma_{su}} [\Psi_i][N][D][B_j] d\Gamma, \end{aligned} \quad (25a)$$

$$f_i = \int_{\Gamma_{st}} [\Psi_i] \bar{t}_i d\Gamma + \int_{\Omega_s} [\Psi_i] b_i d\Omega, \quad (25b)$$

where

$$B_j = \begin{bmatrix} \phi_{j,x} & 0 \\ 0 & \phi_{j,y} \\ \phi_{j,y} & \phi_{j,x} \end{bmatrix}, \quad B_i = \begin{bmatrix} \psi_{i,x} & 0 & \psi_{i,y} \\ 0 & \psi_{i,y} & \psi_{i,x} \end{bmatrix}, \quad N = \begin{bmatrix} n_1 & 0 & n_2 \\ 0 & n_2 & n_1 \end{bmatrix}, \quad (26a)$$

$[\Psi_i]$  is the vector of test functions  $v_j(x)$ . For an isotropic FG linear elastic material the material property matrix  $[D]$  is given by

$$D = \frac{\bar{E}(\mathbf{x})}{1 - \bar{\nu}(\mathbf{x})} \begin{bmatrix} 1 & \bar{\nu}(\mathbf{x}) & 0 \\ \bar{\nu}(\mathbf{x}) & 1 & 0 \\ 0 & 0 & 1 - \bar{\nu}(\mathbf{x}) \end{bmatrix}, \quad (26b)$$

$$\bar{E} = \begin{cases} E, & \bar{\nu} = \begin{cases} \nu & \text{for plane stress,} \\ \frac{\nu}{1-\nu} & \text{for plane strain.} \end{cases} \end{cases} \quad (26c)$$

For plane stress deformations of an orthotropic FG material, we have

$$\begin{aligned} D &= \begin{bmatrix} E_1(\mathbf{x})/e & E_2(\mathbf{x})v_{12}(\mathbf{x})/e & 0 \\ E_2(\mathbf{x})v_{12}/e & E_2(\mathbf{x})/e & 0 \\ 0 & 0 & G_{12}(\mathbf{x}) \end{bmatrix}, \\ e(\mathbf{x}) &= 1 - \frac{E_2(\mathbf{x})}{E_1(\mathbf{x})} (v_{12}(\mathbf{x}))^2. \end{aligned} \quad (26d)$$

For the MLPG5 method with the Heaviside step function taken as the test function, the stiffness matrix and the load vector are given by

$$K_{ij} = - \int_{\Gamma_{st}} [N][D][B_j] d\Gamma - \int_{\Gamma_{su}} [N][D][B_j] d\Gamma, \quad (27a)$$

$$f_i = \int_{\Gamma_{st}} \bar{t}_i d\Gamma + \int_{\Omega_s} b_i d\Omega. \quad (27b)$$

When  $b_i = 0$  then integrals in Eqs. (27a) and (27b) are on parts of the boundary  $\Gamma_s$  of the subdomain  $\Omega_s$ , and the CPU time required to evaluate the stiffness matrix and the load vector is significantly reduced. These line integrals can be evaluated by using an appropriate Gauss quadrature rule by first subdividing  $\Gamma_s$  into several parts and then mapping each segment onto the interval  $[-1, +1]$ . Similarly, integrals on a circular domain in Eq. (25) are computed by mapping it onto a square region.

Since the line and the domain integrals as well as the RBFs are computed without using any mesh, the method is truly meshless. For each Gauss quadrature point  $\mathbf{x}_Q$ , the approximate form of function  $u$  given by Eq. (1) and the corresponding RBFs are found. Thus the evaluation of the stiffness matrix  $K$  and the load vector can be computationally expensive. However, no assembly of equations is needed. The RBFs determine how displacements of node  $i$  affect those of point  $\mathbf{x}_Q$ .

We note that, for every node  $x_i$ , there are two local domains: the test function domain  $\Omega_{ie}^i$  (same as the local subdomain  $\Omega_s$ ) for  $v_i \neq 0$  (of radius  $r_s$ ), and the interpolation domain  $\Omega_i$  for  $\mathbf{x}_Q$  (size  $r_i$ ). Fig. 1 shows the subdomain  $\Omega_s$  of node  $\mathbf{x}_i$  and the interpolation domain  $\Omega_i$  for the integration point  $\mathbf{x}_Q$ . These two circular domains are independent of each other and have radii  $r_s = \alpha_s d_i$  and  $r_i = \alpha_i d_i$ , respectively, where  $\alpha_s$  and  $\alpha_i$  are scaling parameters and  $d_i$  is the distance from the node  $i$  to its closest neighbouring node. The number of nodal variables coupled in Eq. (24) depends upon the size  $r_i$  of the interpolation domain  $\Omega_i$ .

The choice  $v_i(x) = (\delta_{i1} + \delta_{i2})W$  for  $i = 1$  and 2 in Eq. (21) gives two linearly independent equations. Here,  $\delta_{ij}$  is the Kronecker delta. Repeating the procedure for every node in the domain  $\Omega$  gives the following system of simultaneous linear algebraic equations for the solution of nodal displacements.

$$Ku = f. \quad (28)$$

Since shape functions constructed with RBFs possess the Kronecker delta function property, thus essential boundary conditions can be easily satisfied by modifying Eq. (28) and terms in the row of the matrix  $K$  for the nodes where essential boundary conditions are prescribed are not computed to economise on the computing cost.

### 3.2. MLPG method for transient deformations of an anisotropic linear viscoelastic body

Transient deformations of an inhomogeneous body are governed by

$$\sigma_{ij,j}(\mathbf{x}, t) - \rho(\mathbf{x})\ddot{u}_i(\mathbf{x}, t) = -b_i(\mathbf{x}, t), \quad (29)$$

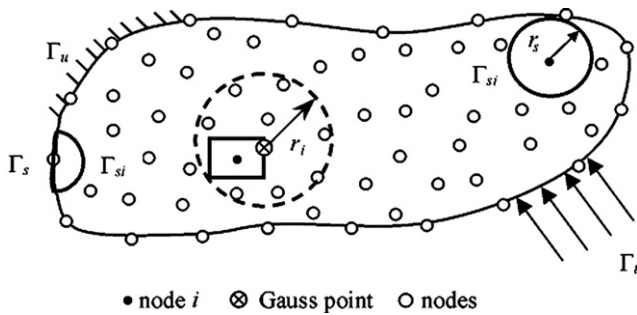


Fig. 1. The support and the interpolation domains: the region enclosed by a circle of radius  $r_s$  equals the support of node  $i$  and that enclosed by the dotted circle of radius  $r_i$  represents the interpolation domain. The two domains are shown separately for clarity.

where  $\rho$  is the mass density,  $\sigma_{ij}(\mathbf{x}, t)$  is the stress tensor,  $u_i(\mathbf{x}, t)$  is the displacement vector, and a dot over a quantity represents its differentiation with respect to time  $t$ . Eq. (18) governing static deformations can be derived from Eq. (29) by setting the acceleration term  $\ddot{u}_i(\mathbf{x}, t)$  equal to zero. The following boundary and initial conditions are assumed:

$$u_i(\mathbf{x}, t) = \tilde{u}_i(\mathbf{x}, t) \text{ on } \Gamma_u, t_i(\mathbf{x}, t) = \tilde{t}_i(\mathbf{x}, t) \text{ on } \Gamma_t, \quad (30a)$$

$$u_i(\mathbf{x}, t)|_{t=0} = u_i(\mathbf{x}, 0) \text{ and } \dot{u}_i(\mathbf{x}, t)|_{t=0} = \dot{u}_i(\mathbf{x}, 0) \text{ in } \Omega. \quad (30b)$$

The constitutive relation for an isotropic linear viscoelastic body can be written as

$$s_{ij} = 2 \int_0^t \mu(\mathbf{x}, t - \tau) \frac{de_{ij}}{d\tau} d\tau, \quad (31a)$$

$$\sigma_{kk} = 3 \int_0^t K(\mathbf{x}, t - \tau) \frac{d\epsilon_{kk}}{d\tau} d\tau, \quad (31b)$$

where  $K$  and  $\mu$  are the bulk and the shear relaxation functions respectively,  $e_{ij}$  is the strain tensor for infinitesimal deformations, and  $s_{ij}$  and  $e_{ij}$  are deviatoric components of the stress and strain tensors, respectively. That is

$$s_{ij} = \sigma_{ij} - \frac{1}{3} \sigma_{kk} \delta_{ij}, \quad (32a)$$

$$e_{ij} = \epsilon_{ij} - \frac{1}{3} \epsilon_{kk} \delta_{ij}. \quad (32b)$$

For an anisotropic linear viscoelastic body Eq. (31) becomes

$$\sigma_{ij}(\mathbf{x}, t) = \int_0^t c_{ijkl}(\mathbf{x}, t - \tau) \frac{d\epsilon_{kl}}{d\tau} d\tau. \quad (33)$$

Here, the relaxation function  $c_{ijkl}(\mathbf{x}, t)$  is assumed to have the form

$$c_{ijkl}(\mathbf{x}, t) = c_0 \tilde{c}_{ijkl}(\mathbf{x}) f(t), \quad (34)$$

where  $c_0$  is a material constant, and  $\tilde{c}_{ijkl}(\mathbf{x})$  and  $f(t)$  depend on the Cartesian coordinates and the time, respectively. Eq. (34) implies that the same relaxation function holds for all components of the tensor  $c_{ijkl}(\mathbf{x}, t)$  that simplifies the analysis considerably. The correspondence principle holds for an inhomogeneous viscoelastic solid [51]. In general, the correspondence principle [51] states that the Laplace transforms of the non-homogeneous viscoelastic variables are obtained by replacing  $c_0$  with  $c_0 p f(p)$ , where  $f(p)$  is the Laplace transform of  $f(t)$ .

Substitution from Eq. (34) into Eq. (33) gives

$$\sigma_{ij}(\mathbf{x}, t) = c_0 \tilde{c}_{ijkl}(\mathbf{x}) \int_0^t f(t - \tau) \frac{d\epsilon_{kl}}{d\tau} d\tau. \quad (35)$$

Taking the Laplace transform of Eqs. (29) and (35) we obtain

$$\bar{\sigma}_{ij,j}(\mathbf{x}, p) - \rho(\mathbf{x}) p^2 \bar{u}_i(\mathbf{x}, p) = -\bar{F}_i(\mathbf{x}, p), \quad (36a)$$

$$\bar{\sigma}_{ij}(\mathbf{x}, p) = c_0 \tilde{c}_{ijkl} p \bar{f}(p) \bar{\epsilon}_{kl}(\mathbf{x}, p), \quad (36b)$$

where

$$\bar{F}_i(\mathbf{x}, p) = b_i(\mathbf{x}, p) + \rho(\mathbf{x}) p u_i(\mathbf{x}, 0) + \rho(\mathbf{x}) \dot{u}_i(\mathbf{x}, 0) \quad (37)$$

combines the effect of initial conditions with the Laplace transform of the body force. Proceeding as in Section 3.1, we obtain the following for the local weak form of Eq. (36a):

$$-\int_{\Gamma_s} \bar{\sigma}_{ij}(\mathbf{x}, p) n_j(\mathbf{x}) v_i(\mathbf{x}) d\Gamma + \int_{\Omega_s} \bar{\sigma}_{ij}(\mathbf{x}, p) v_{i,j}(\mathbf{x}) d\Omega + \int_{\Omega_s} [\rho(\mathbf{x}) p^2 \bar{u}_i(\mathbf{x}, p) + \bar{F}_i(\mathbf{x}, p)] v_i(\mathbf{x}) d\Omega = 0. \quad (38)$$

Substitution of the trial solution and test function discussed above results in the following equation for the MLPG1 formulation:

$$\begin{aligned} & -\sum_{i=1}^n u^i(p) \int_{\Gamma_{st}} \Psi(\mathbf{x}) \mathbf{N}(\mathbf{x}) \bar{\mathbf{D}}(\mathbf{x}, p) \mathbf{B}(\mathbf{x}) d\Gamma \\ & + \sum_{i=1}^n u^i(p) \int_{\Omega_s} \tilde{\mathbf{B}}(\mathbf{x}) \bar{\mathbf{D}}(\mathbf{x}, p) \mathbf{B}(\mathbf{x}) d\Omega \\ & + p^2 \sum_{i=1}^n u^i(p) \int_{\Omega_s} \rho(\mathbf{x}) \psi(\mathbf{x}) \phi(\mathbf{x}) d\Omega \\ & - \sum_{i=1}^n u^i(p) \int_{\Gamma_{su}} \Psi(\mathbf{x}) \mathbf{N}(\mathbf{x}) \bar{\mathbf{D}}(\mathbf{x}, p) \mathbf{B}(\mathbf{x}) d\Gamma \\ & = \int_{\Gamma_{st}} \Psi(\mathbf{x}) \bar{\mathbf{t}}(\mathbf{x}, p) d\Gamma + \int_{\Omega_s} \Psi(\mathbf{x}) \bar{\mathbf{F}}(\mathbf{x}, p) d\Omega. \end{aligned} \quad (39)$$

For the MLPG5 formulation, we get

$$\begin{aligned} & -\sum_{i=1}^n u^i(p) \int_{\Gamma_{st}} \mathbf{N}(\mathbf{x}) \bar{\mathbf{D}}(\mathbf{x}, p) \mathbf{B}(\mathbf{x}) d\Gamma \\ & + p^2 \sum_{i=1}^n u^i(p) \int_{\Omega_s} \rho(\mathbf{x}) \phi(\mathbf{x}) d\Omega \\ & - \sum_{i=1}^n u^i(p) \int_{\Gamma_{su}} \mathbf{N}(\mathbf{x}) \bar{\mathbf{D}}(\mathbf{x}, p) \mathbf{B}(\mathbf{x}) d\Gamma \\ & = \int_{\Gamma_{st}} \bar{\mathbf{t}}(\mathbf{x}, p) d\Gamma + \int_{\Omega_s} \bar{\mathbf{F}}(\mathbf{x}, p) d\Omega. \end{aligned} \quad (40)$$

Eqs. (39) or (40) are solved for nodal displacements in the Laplace transformed domain. The time-dependent nodal values are determined by taking the inverse Laplace transforms of Eqs. (39) and (40) with Stehfest's inversion algorithm [52]. According to this algorithm, at time  $t$ , an approximate value  $f_a$  of the function  $f(t)$  is given by

$$f_a(t) = \frac{\ln 2}{t} \sum_{i=1}^N v_i \bar{f}\left(\frac{\ln 2}{t} i\right), \quad (41)$$

where

$$v_i = (-1)^{N/2+i} \sum_{k=\lfloor (i+1)/2 \rfloor}^{\min(i, N/2)} \frac{k^{N/2} (2k)!}{(N/2 - k)! k! (k-1)! (i-k)! (2k-i)!} \quad (42)$$

The accuracy and computational efficiency of the algorithm depend on the value of  $N$  in Eq. (41). In order to obtain the solution at time  $t$ , one needs to solve  $N$  boundary-value problems in the Laplace-transform para-

meter  $p = i \ln 2 / t$ . Sladek et al. [30] and Sutradhar et al. [53] achieved good accuracy with  $N = 10$ , and for the numerical examples discussed below we also take  $N = 10$ . For the transient heat conduction problem, Vel and Batra [54] employed 15 terms, expressed the solution in the Laplace transformed domain in terms of the partial fractions of  $p$ , and then took its inverse.

#### 4. Determination of effective material properties of an FGM

One can presume closed form expressions for the variation of elastic moduli and then find the required volume fractions of constituents which may be difficult to achieve experimentally. Simple expressions facilitate solving analytically the pertinent boundary-value problem. Alternatively, one employs a micromechanical analysis to ascertain effective elastic moduli of an FGM from the volume fractions and shapes of constituents. Methods that consider only volume fractions of constituents include the rule of mixtures, the Mori–Tanaka method [55] and the self-consistent approach [56]. For problems studied here, we use either closed-form expressions for the moduli or use the Mori–Tanaka or the self-consistent method to derive them from presumed variations of volume fractions of the constituents. Formulae for the effective moduli in these two techniques are described below.

##### 4.1. Mori–Tanaka method

The effective bulk modulus  $K_e$  and the effective shear modulus  $\mu_e$  of a mixture of two constituents is given by

$$\frac{K_e - K_1}{K_2 - K_1} = \frac{V_2}{1 + (1 - V_2)(3(K_2 - K_1)/(3K_1 + 4\mu_1))}, \quad (43a)$$

$$\begin{aligned} \frac{\mu_e - \mu_1}{\mu_2 - \mu_1} &= \frac{V_2}{1 + (1 - V_2)(\mu_2 - \mu_1)/(\mu_1 + \mu_1(9K_1 + 8\mu_1)/6(K_1 + 2\mu_1))}. \end{aligned} \quad (43b)$$

Here,  $K_1$ ,  $\mu_1$  and  $V_1$  are, respectively, the bulk modulus, the shear modulus and the volume fraction of constituent 1, and  $K_2$ ,  $\mu_2$  and  $V_2 = 1 - V_1$  are the corresponding quantities of constituent 2. The bulk and the shear moduli are related to Young's modulus and Poisson's ratio by

$$K = \frac{E}{3(1 - 2\nu)}, \quad (44a)$$

$$\mu = \frac{E}{2(1 + \nu)}. \quad (44b)$$

##### 4.2. Self-consistent method

For a two-phase composite, the effective bulk and shear moduli are determined from

$$\frac{1}{K + 4/3\mu} = \frac{V_1}{K_1 + 4/3\mu} + \frac{V_2}{K_2 + 4/3\mu}, \quad (45a)$$

$$\frac{V_1 K_1}{K_1 + 4/3\mu} + \frac{V_2 K_2}{K_2 + 4/3\mu} + 5 \left( \frac{V_1 \mu_2}{\mu - \mu_2} + \frac{V_2 \mu_1}{\mu - \mu_1} \right) + 2 = 0. \quad (45b)$$

Note that the quartic equation (45b) needs to be solved for the effective shear modulus  $\mu$ .  $K$  is then computed from Eq. (45a). It is therefore easier to use the Mori–Tanaka method than the self-consistent method. Young’s modulus and Poisson’s ratio are determined as in the Mori–Tanaka method using Eq. (44).

### 5. Numerical examples

Five example problems have been analysed to illustrate the accuracy, efficiency and versatility of the present method. We adopt the optimum values of shape parameters for the MQ–RBFs determined previously [24] as  $c = 6d$  and  $\beta = 1.99$ , where  $d$  equals the minimum distance between two nodes. The scaling parameters for circular subdomains and interpolation domains are assigned values  $\alpha_s = 0.75$  and  $\alpha_i = 3.5$ . We used 6 Gauss points for numerical evaluation of line integrals and a  $6 \times 6$  quadrature scheme (i.e., 36 Gauss points) to evaluate domain integrals. It should be noted that the present RBF MLPG methods are more efficient than the MLS–MLPG methods because it is easier to impose the essential boundary conditions using RBFs.

#### 5.1. Rotating orthotropic FG disc

We first study deformations of a thin orthotropic solid glass/epoxy disc of radius  $R = 1$  m rotating about the  $z$ -axis, which is perpendicular to the disc surface. This problem has been analysed by Sladek et al. [30] with the MLPG5 method using the MLS basis functions to approximate the trial solution. In order to compare our results with those of Sladek et al. [30], we use the same material properties as they did, i.e.,  $E_{10} = 48.26$  GPa,  $E_{20} = 17.24$  GPa,  $G_{12} = 6.89$  GPa,  $\nu_{12} = 0.29$ , and  $\rho_0 = 1$  kg/m<sup>3</sup>. Young’s moduli and the mass density are taken to vary exponentially only in the radial direction according to the relations:

$$\rho(r) = \rho_0 e^{(\gamma r)}, \quad (46a)$$

$$E_i(r) = E_{i0} e^{(\gamma r)}, \quad (46b)$$

where  $\rho_0$  and  $E_{i0}$  are the mass density and Young’s moduli at the centre of the disc, and  $\gamma$  is a scaling parameter. The material principal directions coincide with the  $x$  and  $y$  axes of the disc as shown in Fig. 2 that also depicts a plot of Eq. (46a).

Even though the problem is 1D, we analyse it as 2D in rectangular Cartesian coordinates and deformations of a quarter of the disc are studied. We use the same number and location of nodes as in [30] (95 nodes with 37 located

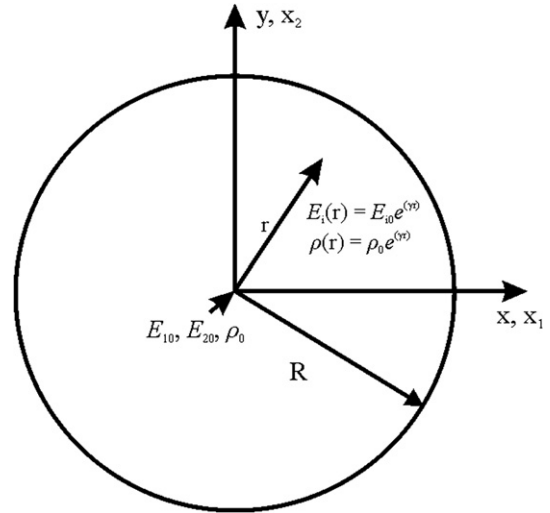


Fig. 2. Schematic of an orthotropic FGM disc showing values of material properties at two points.

on the global boundary). Results are computed for three values, 0.0, 0.1 and 0.3, of the grading parameter  $\gamma$ ;  $\gamma = 0$  corresponds to a homogeneous disc. A disc with constant elastic moduli is first analysed with the mass density varying with the radial distance  $r$  according to Eq. (46a). The presently computed variations along the radial direction of the radial and the hoop stresses, normalised by  $\rho_0 \omega^2 R^2$  where  $\omega$  is the angular speed of the disc, are compared with those of Sladek et al. [30] in Figs. 3 and 4. It can be seen that the present results from the MLPG1 and the MLPG5 formulations are in excellent agreement with those of Sladek et al. [30]. The maximum values of the radial and the hoop stresses occur at the centre of the plate, and as expected are equal to each other. An increase in the mass density (i.e., increasing  $\gamma$ ) enhances both stress components due to the higher centrifugal force on the disc. Variations of displacements, normalised by  $\rho_0 \omega^2 R^3 / E_2$ , and shown

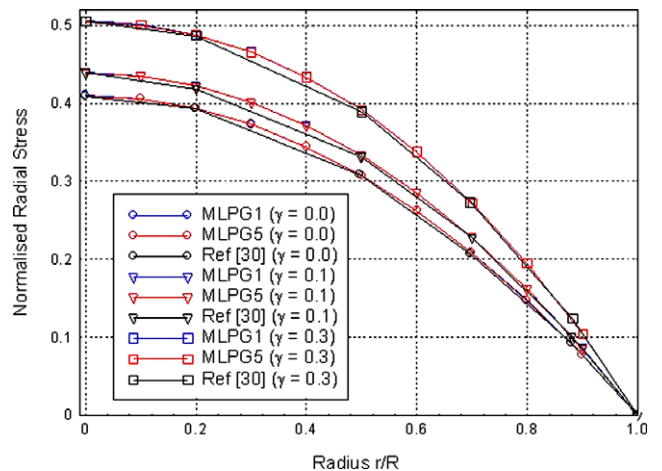


Fig. 3. (Color online) Normalised radial stress vs. the radius in the rotating orthotropic FGM disc with constant elastic moduli and variable mass density.

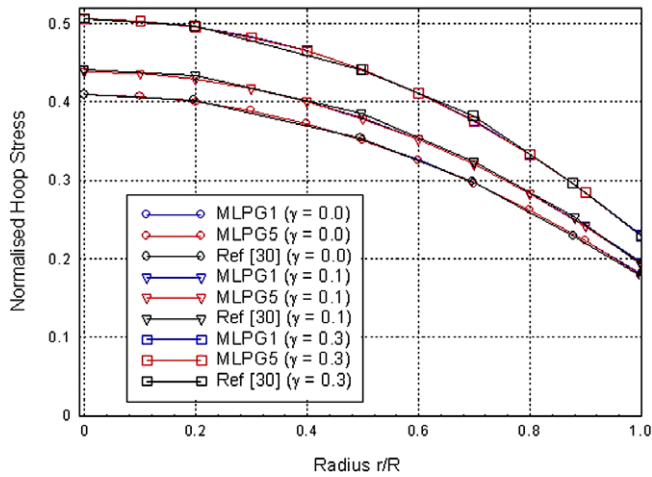


Fig. 4. (Color online) Normalised hoop stress vs. radius in the rotating orthotropic FGM disc with constant elastic moduli and variable mass density.

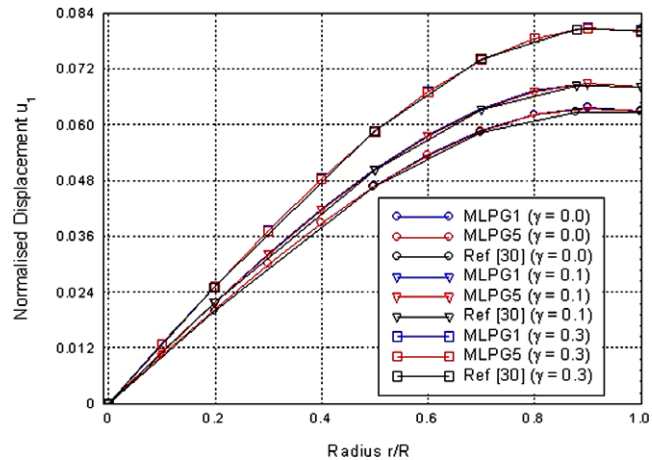


Fig. 5. (Color online) Normalised displacement  $u_1$  vs. radius in the rotating orthotropic FGM disc with constant elastic moduli and variable mass density.

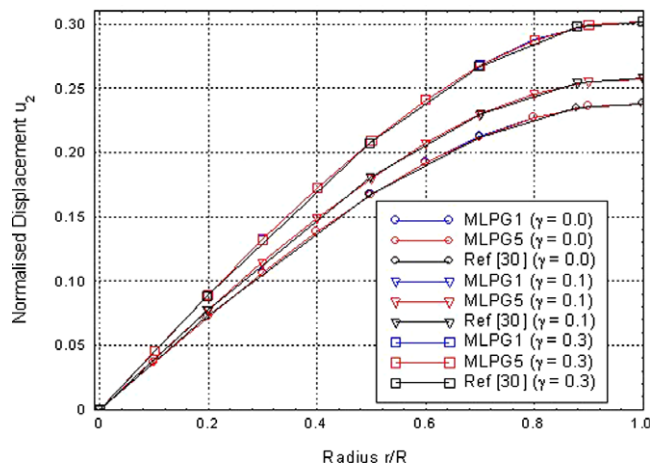


Fig. 6. (Color online) Normalised displacement  $u_2$  vs. radius in the rotating orthotropic FGM disc with constant elastic moduli and variable mass density.

in Figs. 5 and 6 also agree very well with those reported by Sladek et al. [30]. It can be seen that for every value of radius  $r$  the displacement  $u_2$  is much larger than the displacement  $u_1$  because Young's modulus  $E_1$  is greater than  $E_2$  making the plate stiffer in the  $x$ -direction.

We now assume that both elastic moduli and mass density vary with  $r$  according to Eq. (46). Normalised stresses and displacements calculated using the MLPG1 and the MLPG5 formulations and depicted in Figs. 7–10 agree well with those reported by Sladek et al. [30]. A comparison of stresses in Figs. 7 and 8 (variable density and Young's moduli) with those in Figs. 3 and 4 (variable density only) suggests that adding Young's modulus variation to the mass density variation tends to diminish effects of the mass density variation. It should be apparent from results plotted in Fig. 8 that the inhomogeneity in material properties shifts the location of the peak circumferential stress away from the centre of the disc. By comparing displacements plotted in Figs. 9 and 10 with those in Figs. 5 and 6, we conclude that the variation in Young's modulus reduces

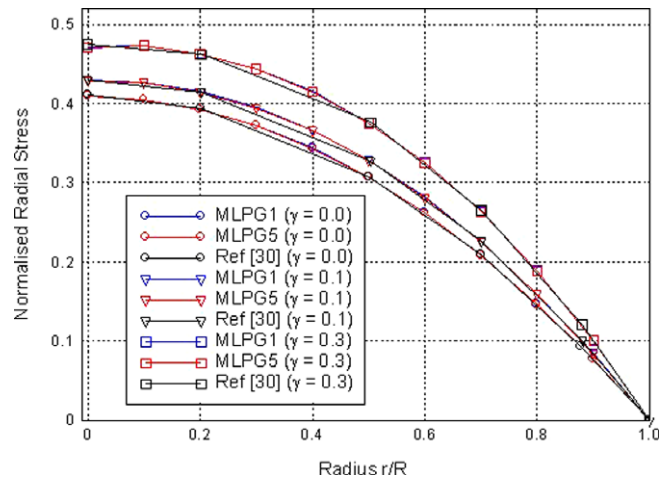


Fig. 7. (Color online) Normalised radial stress vs. radius in the rotating orthotropic FGM disc with variable elastic moduli and mass density.

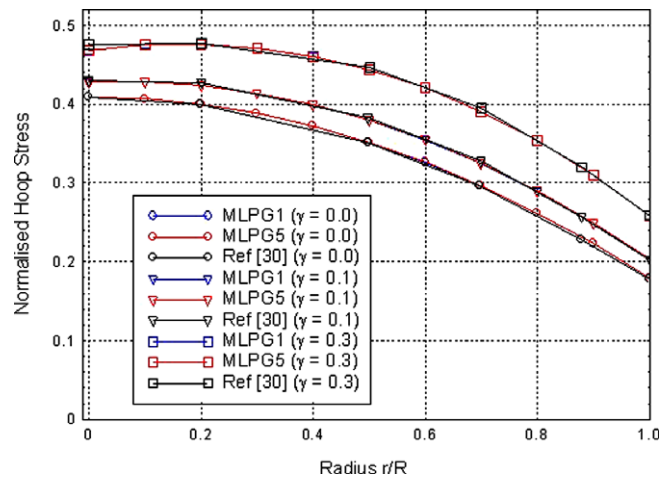


Fig. 8. (Color online) Normalised hoop stress vs. radius in the rotating orthotropic FGM disc with variable elastic moduli and mass density.

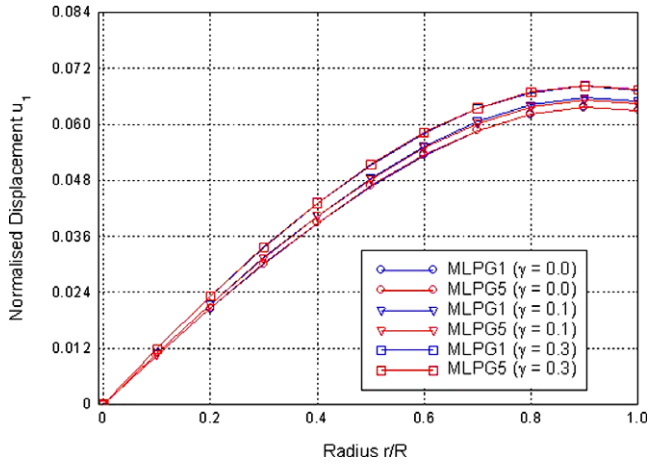


Fig. 9. (Color online) Normalised displacement  $u_1$  vs. radius in the rotating orthotropic FGM disc with variable elastic moduli and mass density.

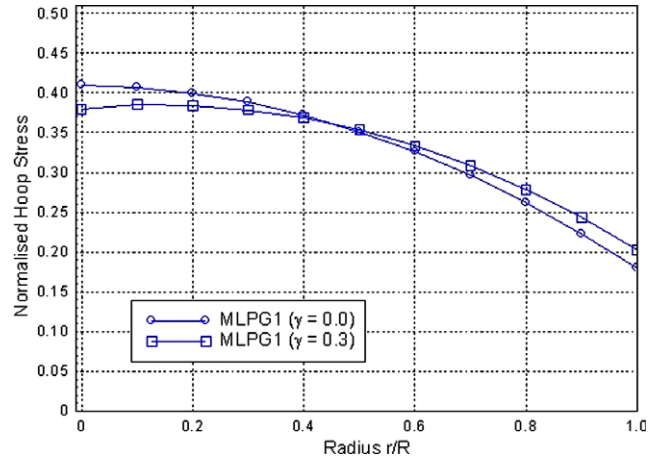


Fig. 12. Normalised hoop stress vs. radius in the rotating orthotropic FGM disc with variable elastic moduli and constant mass density.

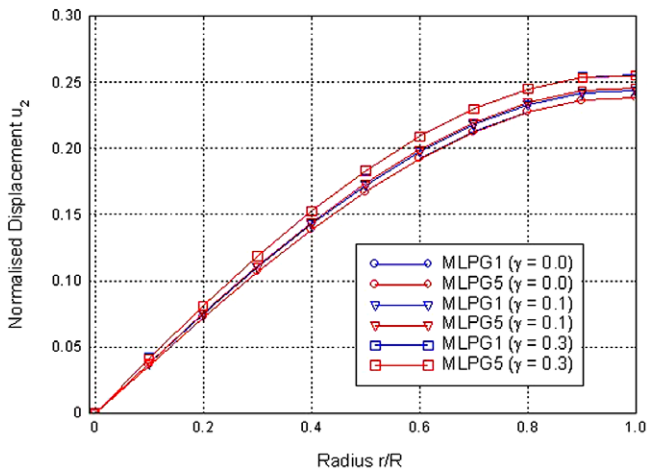


Fig. 10. (Color online) Normalised displacement  $u_2$  vs. radius in the rotating orthotropic FGM disc with variable elastic moduli and mass density.

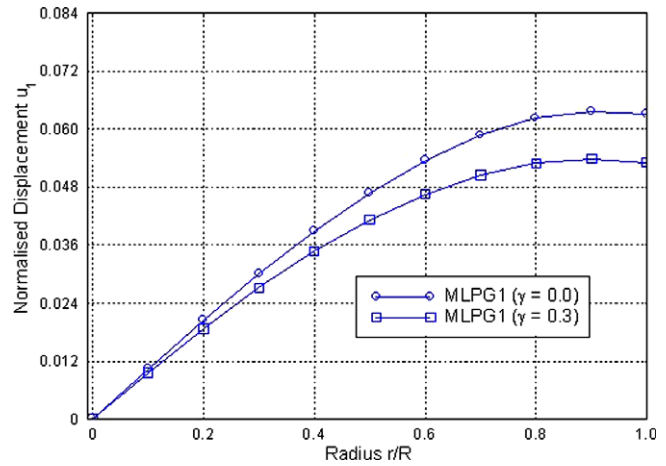


Fig. 13. Normalised displacement  $u_1$  vs. radius in the rotating orthotropic FGM disc with variable elastic moduli and constant mass density.

the magnitudes of  $u_1$  and  $u_2$ . These conclusions are further supported by results plotted in Figs. 11–14, where stresses and displacements are plotted for  $\gamma = 0$  and 0.3 using the

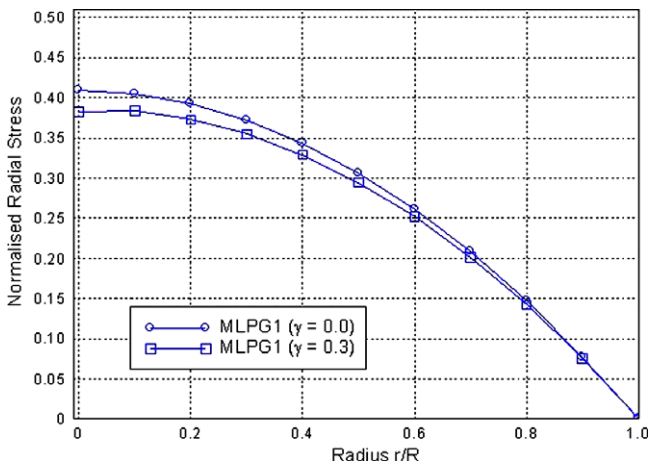


Fig. 11. Normalised radial stress vs. radius in the rotating orthotropic FGM disc with variable elastic moduli and constant mass density.

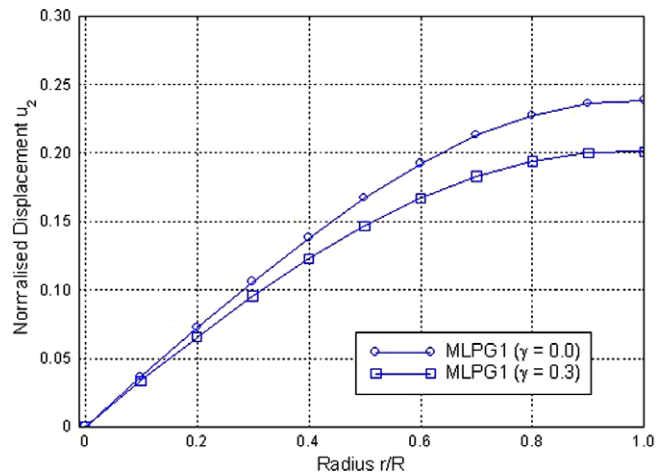


Fig. 14. Normalised displacement  $u_2$  vs. radius in the rotating orthotropic FGM disc with variable elastic moduli and constant mass density.

MLPG1 method with varying Young’s moduli only (constant mass density). These results imply that increasing Young’s moduli leads to decreased displacements as would

be expected since the disc is stiffer. The effect on the circumferential stress plotted in Fig. 12 is more involved, with the value at the centre of the disc decreasing with increasing Young’s moduli, and that at the outer edge increasing. This leads to the shift in the location of the peak circumferential stress away from the centre of the disc, as seen in Fig. 8.

5.2. Rotating viscoelastic FG disc

For this problem also studied by Sladek et al. [30], we assume that Young’s moduli vary with both time and spatial coordinates according to the following relation:

$$E_i(\mathbf{x}, t) = E_{i0}e^{(\gamma r)}f(t) \\ = E_{i0}e^{(\gamma r)}\left[\frac{E_{i\infty}}{E_{i0}} + \left(1 - \frac{E_{i\infty}}{E_{i0}}\right)\exp\left(-\frac{t}{t_0}\right)\right]. \quad (47)$$

The shear modulus  $G_{12}$  is also assumed to be given by an equation analogous to Eq. (47). However, the mass density is kept constant. Values assigned to material parameters are:  $E_{10} = 48.26$  GPa,  $E_{20} = 17.24$  GPa,  $G_{120} = 6.89$  GPa,  $E_{1\infty} = 15$  GPa,  $E_{2\infty} = 6$  GPa,  $G_{12\infty} = 2$  GPa,  $t_0 = 2.5$  s,  $\nu_{12} = 0.29$ . According to the correspondence principle [51], Young’s moduli  $E_{i0}e^{(\gamma r)}$  in the corresponding elastic analysis should be replaced by

$$E_{i0}e^{(\gamma r)}p\bar{f}(p) = [E_{i\infty} + (E_{i0} - E_{i\infty})\frac{pt_0}{pt_0 + 1}]e^{(\gamma r)}. \quad (48)$$

The problem has been analysed with zero initial conditions, i.e.,  $u_i(\mathbf{x}, 0) = \dot{u}_i(\mathbf{x}, 0) = 0$ . Fig. 15 compares time histories of the presently computed displacements at  $r = R$ , normalised by  $\rho_0\omega^2R^3/E_{20}$ , with those of Sladek et al. [30]. It can be concluded that both MLPG1 and MLPG5 formulations give equally good results that are in excellent agreement with those of Sladek et al. [30]. It should be noted that because of the domain integral on the left-hand side of Eq. (40), the MLPG5 formulation no longer has only line integrals and hence is not advantageous over the MLPG1 formulation for a dynamic problem.

5.3. A pressurised hollow FG cylinder

Fig. 16 exhibits a schematic sketch of the problem that has also been studied by Ching and Yen [28] with the MLPG1 method using the MLS basis functions to approximate the trial solution. The cylinder made of an isotropic material with inner radius  $r_a = 5$  mm and outer radius  $r_b = 10$  mm is subjected to pressure on either its internal or external surface. The variation of Young’s modulus of the cylinder material in the radial direction is given by

$$E(\bar{r}) = E_0\bar{r}^\eta, \quad (49)$$

where  $\bar{r} = r/r_a$ ,  $E_0 = 1$  unit and the parameter  $\eta$  controls the profile of the material gradation with radial coordinate;  $\eta = 0$  for a homogeneous cylinder. Poisson’s ratio,  $\nu = 0.3$ , is taken to be a constant. A plane strain state of deformation is assumed, and due to the symmetry of the problem

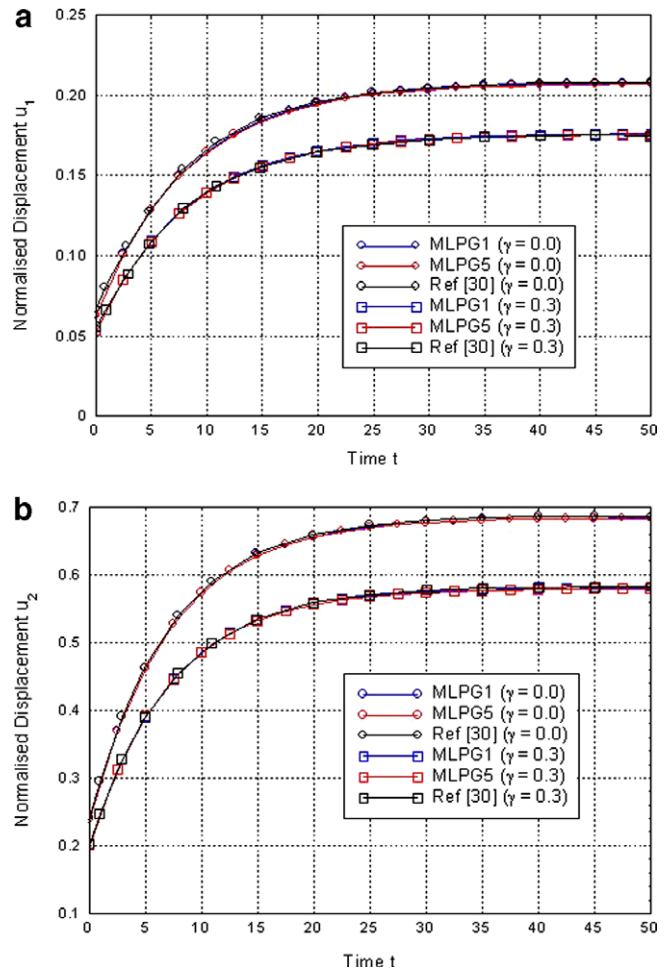


Fig. 15. (Color online) Time variation of normalised displacements at a point on the outermost surface of a rotating viscoelastic FG disc. (a) Normalised displacement  $u_1$  and (b) normalised displacement  $u_2$ .

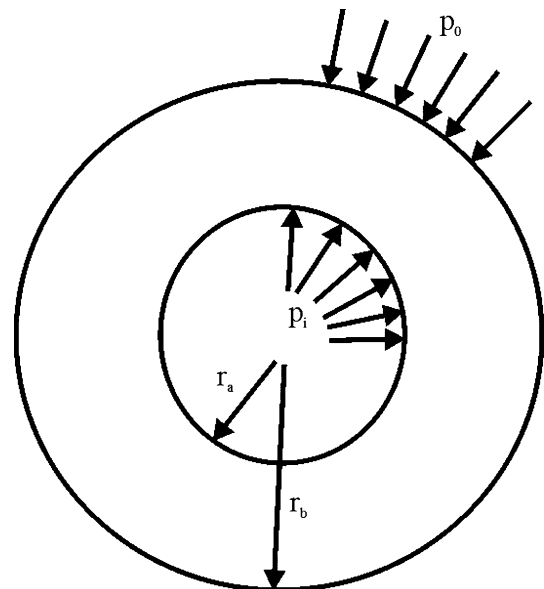


Fig. 16. Schematic sketch of the FG cylinder under applied pressure.

about the horizontal and the vertical axes, deformations of only a quarter of the cylinder are analysed. Results with the MPLG1 and the MLPG5 formulations using 840 nodes are compared with the closed form solution of Horgan and Chan [47]. Since the two MLPG methods give almost identical values of the radial and the hoop stresses, for brevity, we have displayed radial stresses computed with the MLPG1 method and hoop stresses with the MLPG5 formulation. For different values of  $\eta$ , as shown in Figs. 17 and 18, the computed radial the hoop stresses normalised by the applied pressure match well with those from the analytical solution [47]. For all values of  $\eta$  considered, the radial stress increases monotonically with the radius  $r$  whereas the hoop stress does not. The radial stress distribution is quadratic for  $\eta = 0$  in agreement with the classical result for a homogeneous cylinder, but becomes increasingly linear as  $\eta$  increases. This is because with an increase in  $\eta$  the cylinder becomes increasingly stiff towards the outer edge resulting in the compressive radial stress increasing

more rapidly from the outer surface to the inner surface as compared to that for  $\eta = 0$ . For  $\eta = 0$  and  $\eta = 1$ , the maximum hoop stress occurs at a point on the inner surface but for  $\eta = 2$  and  $\eta = 3$ , the maximum hoop stress is at a point on the outer surface of the cylinder. Results for an externally loaded cylinder are shown in Figs. 19 and 20; both the radial and the hoop stresses are compressive as expected and agree very well with their corresponding analytical values. We note that as for deformations of the disc analysed in Sections 5.1 and 5.2, it is basically 1D problem even though it has been studied as 2D in rectangular Cartesian coordinates.

5.4. Pressurised FG cylinder with material properties calculated by the Mori–Tanaka and the self-consistent schemes

The pressurised cylinder of Section 5.3 is now taken to be comprised of aluminium (Al) and ceramic (SiC) with the following material properties:

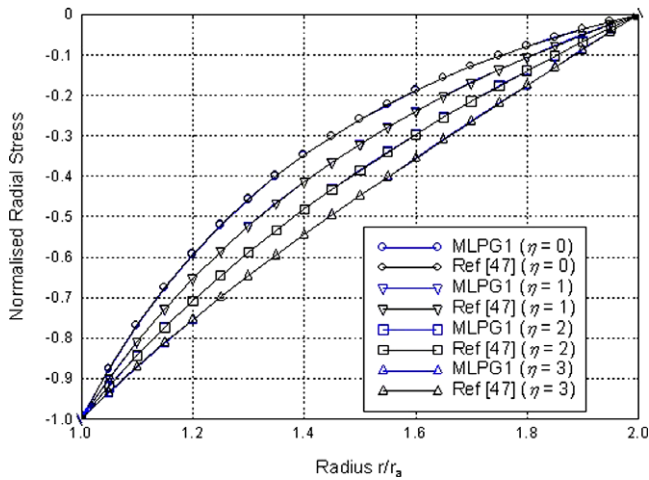


Fig. 17. (Color online) Normalised radial stress vs. radius in the pressurised hollow FG cylinder under internal pressure.

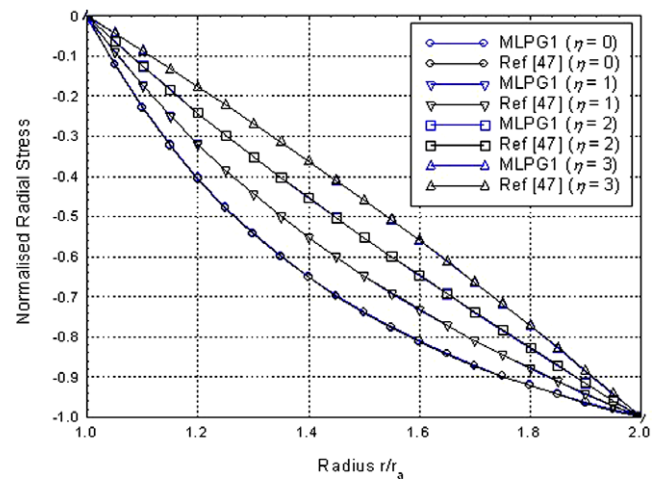


Fig. 19. (Color online) Normalised radial stress vs. radius in the pressurised hollow FG cylinder under external pressure.

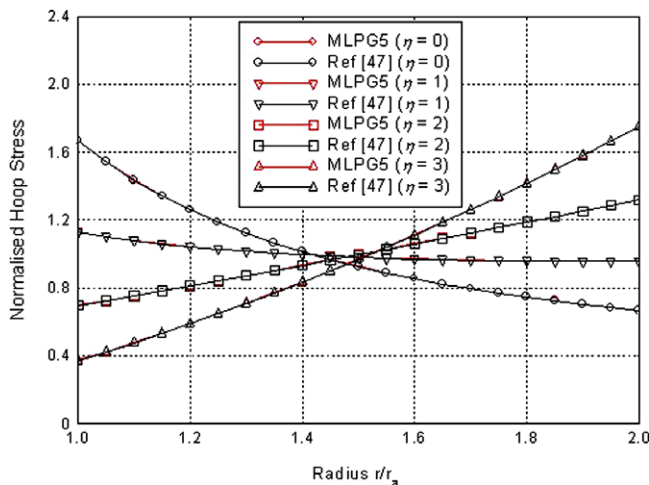


Fig. 18. (Color online) Normalised hoop stress vs. radius in the pressurised hollow FG cylinder under internal pressure.

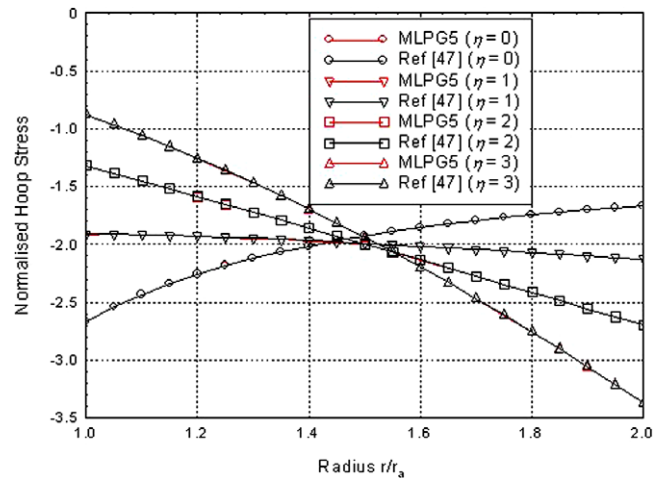


Fig. 20. (Color online) Normalised hoop stress vs. radius in the pressurised hollow FG cylinder under external pressure.

Al :  $E = 70 \text{ GPa}$   $\nu = 0.3$ ,  
 SiC :  $E = 427 \text{ GPa}$   $\nu = 0.17$ .

The volume fraction of the ceramic is assumed to be given by

$$V_c = V_c^o + (V_c^o - V_c^i) \left( \frac{r - r_a}{r_b - r_a} \right)^\eta, \quad (50)$$

where  $V_c^o$  and  $V_c^i$  are, respectively, volume fractions of the ceramic on the outer and the inner surfaces of the cylinder, and  $\eta$  is the power law index that controls the inhomogeneity of the material phases through the thickness. The effective material properties at a point are calculated using Eq. (43) for the Mori–Tanaka method, and Eq. (45) for the self-consistent method. For an internally loaded cylinder with  $V_c^o = 1.0$  and  $V_c^i = 0.0$  variations with  $r$  of the radial and the hoop stresses for different values of  $\eta$  are plotted in Figs. 21 and 22. As in the previous section, the radial stress and the hoop stress values are from solutions with the MLPG1 and the MLPG5 methods, respectively. The presently computed results agree very well with those of Ching and Yen [28] who used the MLPG1 method and the MLS basis functions to approximate the trial solution. For both schemes of finding effective material properties, variations with  $r$  of the radial stress for  $1 < \eta < 3$  are virtually unchanged. The difference between results calculated with the Mori–Tanaka and the self-consistent schemes is more apparent in the hoop stresses plotted in Fig. 22. The change in  $\eta$  from 1 to 3 increases the magnitude of the hoop stress on the inner and the outer surfaces of the cylinder.

Variations of the radial and the hoop stresses with the change in the volume fraction of the ceramic phase on the inner surface of the cylinder are plotted in Figs. 23 and 24. As the volume fraction of the ceramic phase on the inner surface increases the volume fraction of the cera-

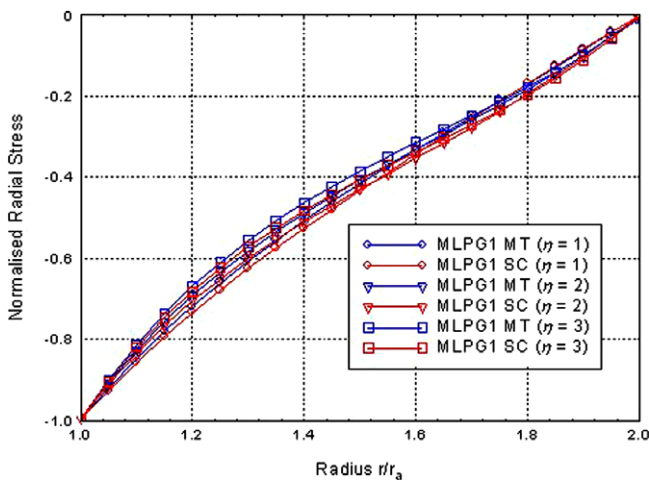


Fig. 21. (Color online) Normalised radial stress vs. radius in the pressurised hollow FG cylinder under internal pressure: material variation through radial direction determined using Mori–Tanaka (MT) and self-consistent (SC) methods ( $V_c^o = 1, V_c^i = 0$ ).

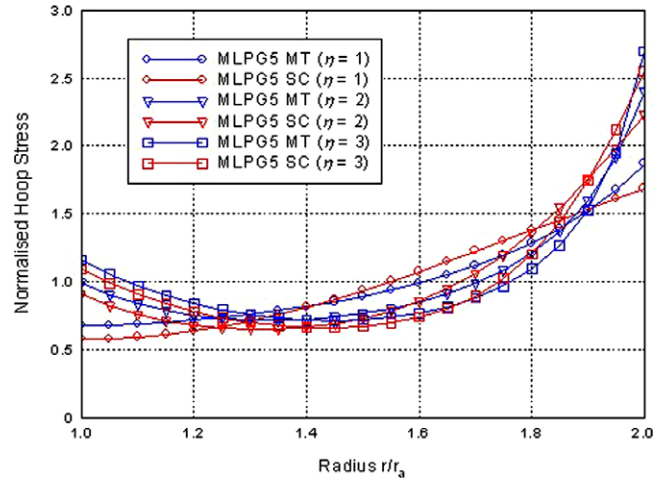


Fig. 22. (Color online) Normalised hoop stress vs. radius in the pressurised hollow FG cylinder under internal pressure: material moduli in the radial direction determined using Mori–Tanaka (MT) and self consistent (SC) methods ( $V_c^o = 1, V_c^i = 0$ ).

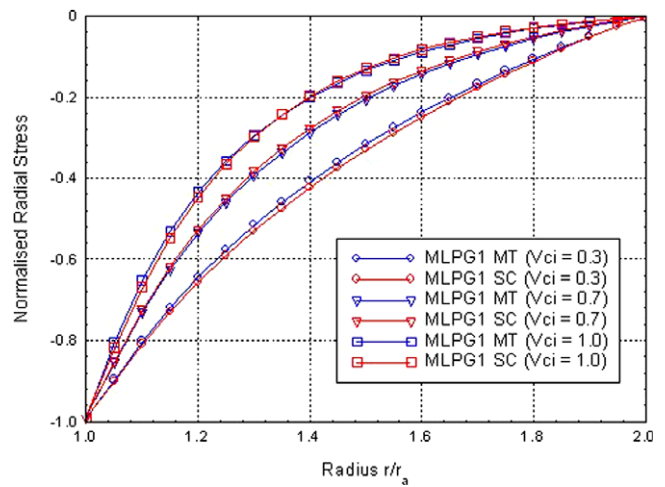


Fig. 23. (Color online) Normalised radial stress vs. radius in the internally pressurised hollow FG cylinder for different volume fractions of ceramic on the inner surface of the cylinder:  $\eta = 1$ , material moduli in the radial direction determined using Mori–Tanaka (MT) and self-consistent (SC) methods.

mic phase on the outer surface decreases according to the relation  $V_c^o = 1 - V_c^i$ . It can be seen that as the volume fraction of the ceramic on the inner surface of the cylinder is increased from 0 to 1 the distribution of the radial stress becomes increasingly non-linear. The hoop stress increases on the inner surface and decreases on the outer surface as the ceramic content shifts to the inner surface, resulting in a change in the location of the maximum hoop stress from the outer to the inner surface.

### 5.5. FG link bar

The FG link bar, shown in Fig. 25, made of titanium/titanium monoboride is subjected to a tensile load of 1 unit

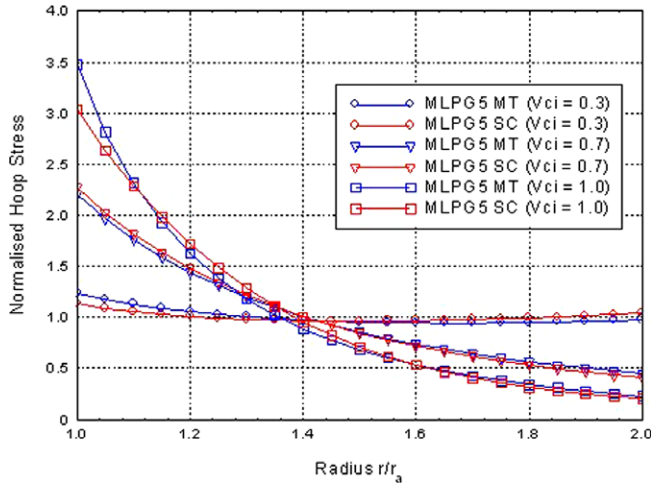


Fig. 24. (Color online) Normalised hoop stress vs. radius in the internally pressurised hollow FG cylinder for different volume fractions of ceramic on the inner surface of the cylinder:  $\eta = 1$ , material moduli in the radial direction determined using Mori–Tanaka (MT) and self-consistent (SC) methods.

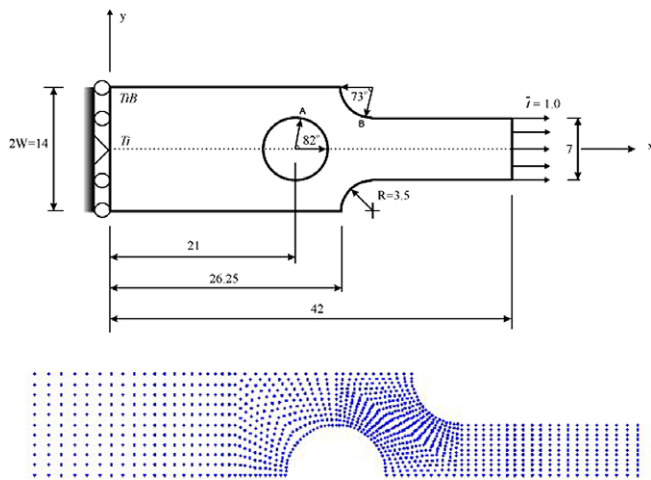


Fig. 25. Schematic of a link bar and the locations of 1101 nodes.

at the right edge. Values assigned to material parameters of titanium monoboride (TiB) and titanium (Ti) are

$$E_{\text{TiB}} = 375 \text{ GPa}, \quad \nu_{\text{TiB}} = 0.14, \quad E_{\text{Ti}} = 107 \text{ GPa}, \quad \nu_{\text{Ti}} = 0.34.$$

These properties are assumed to vary exponentially in the  $y$ -direction according to the following relations:

$$E(y) = E_{\text{Ti}} e^{\beta_E y}, \tag{51a}$$

$$\nu(y) = \nu_{\text{Ti}} e^{\beta_\nu y}, \tag{51b}$$

where the non-homogeneity parameters  $\beta_E$  and  $\beta_\nu$  are given by

$$\beta_E = \frac{1}{W} \log(E_{\text{TiB}}/E_{\text{Ti}}), \tag{52a}$$

$$\beta_\nu = \frac{1}{W} \log(\nu_{\text{TiB}}/\nu_{\text{Ti}}). \tag{52b}$$

Due to the symmetry of the problem about the  $x$ -axis, deformations of the upper half of the bar with 1101 nodes

Table 1

Comparison of presently computed axial stresses at points A and B in Fig. 25 with those given in [28,57]

Method	Material properties	Location A	Location B
MLS-MLPG1 [28]	Homogeneous	2.918	2.140
	FGM	2.360	2.594
Graded FEM [57]	Homogeneous	2.908	2.137
	FGM	2.369	2.601
RBF-MLPG1	Homogeneous	2.885	2.127
	FGM	2.420	2.620
RBF-MLPG5	Homogeneous	2.901	2.131
	FGM	2.403	2.607

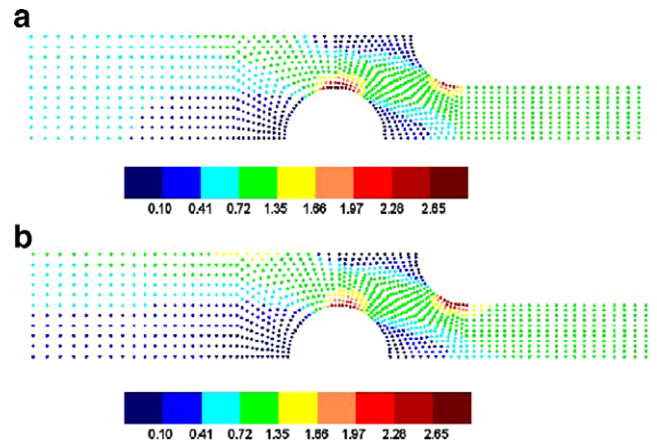


Fig. 26. (Color online) Contours of the axial stress  $\sigma_{xx}$  for a homogeneous and a FG link bar. (a) Homogeneous and (b) FGM.

located as shown in Fig. 25 are found. The problem under the assumption of plane stress state of deformation has been analysed by Ching and Yen [28] and Kim and Paulino [57] who found that the use of a FG material reduces stress concentration and changes the location of the maximum axial stress in the bar. For a homogeneous isotropic bar, they [28,57] found that the maximum axial stress occurs at point A in Fig. 25, and for a bar made of a FG material the maximum stress occurs at point B. As values of the axial stress ( $\sigma_{xx}$ ) listed in Table 1 show, the presently computed axial stress agrees very well with that reported in [28,57]. Contour plots of the axial stress, calculated using the MLPG5 formulation, are shown in Fig. 26 for a homogenous and a FG bar. It is clear from these plots that for a homogeneous material, the maximum axial stress is at point A, but for a FG bar it is at point B and is also reduced compared to that in the homogeneous bar.

## 6. Remarks

All problems discussed above are linear and solutions are valid for infinitesimal deformations of FG bodies. Batra [58] and Love and Batra [59,60] have incorporated material and geometric nonlinearities in the analysis of problems for FG hyperelastic and elasto-thermo-viscoplastic bodies, respectively. Zhang and Batra [61] have used the MSPH method to study wave propagation in a linear elastic FG bar.

One can avoid using the correspondence principle in the analysis of FG viscoelastic bodies by differentiating with respect to time the constitutive relation (31) and expressing it as an ordinary differential equation, e.g., see [62]. It introduces stresses as additional unknowns at nodes but allows for a general variation of material moduli.

## 7. Conclusions

Two MLPG formulations, namely the MLPG1 and the MLPG5, using the multiquadric radial basis function to approximate the trial solution have been used to analyse 2D problems for isotropic and orthotropic FG structures. In the MLPG1 formulation, the test function is taken as the fourth order spline and in the MLPG5 method it equals the Heaviside step function. In each case, the weak form of governing equations is derived on a subdomain of the given domain, and domain integrals are evaluated without using any background mesh. Thus, no element connectivity is needed and the two methods are truly meshless. The shape functions constructed using the RBF interpolation satisfy the Kronecker delta property; thus no special procedure is needed to satisfy essential boundary conditions. The spatial variation of material properties is either taken to be known a priori or derived from the known volume fractions of constituents by using either the Mori–Tanaka or the self-consistent schemes. For a body made of a FG viscoelastic material, governing equations transformed to the Laplace domain are solved numerically and their inverse Laplace transform taken using Stehfest's algorithm.

It is found that for the five 2D problems studied the MLPG1 and the MLPG5 methods with basis functions derived by using the RBFs yield results that are in excellent agreement with those from either the analytical solutions of the problems or numerical solutions of others who employed a different set of basis functions to approximate the trial solution. An advantage of using the MLPG5 method over the MLPG1 method in static problems is that in the absence of body forces only line integrals appear in the weak formulation. These line integrals can be easily evaluated numerically. However this advantage is lost in time-dependent problems solved by using the Laplace-transform technique.

Results for the five example problems studied herein suggest that the deformation and the stress distributions in a functionally graded structure differ considerably from those in the corresponding homogeneous bodies. Thus, a properly tailored FG structure can yield significant advantages over its homogeneous counterpart, such as lower deflection, redistributed deflection and stress fields, and reduced stress concentrations.

## Acknowledgements

D.F.G gratefully acknowledges the support of the Irish Research Council for Science, Engineering and Technology Embark postgraduate scholarship scheme. RCB's work

was partially supported by the ONR grant N00014-1-06-0567 to Virginia Polytechnic Institute and State University with Dr. Y.D.S. Rajapakse as the program manager. Views expressed herein are those of authors and neither of funding agencies nor of their institutions.

## References

- [1] R. Berger, P. Kwon, C.K.H. Dharan, High speed centrifugal casting of metal matrix composites, in: *The Fifth International Symposium on Transport Phenomena and Dynamics of Rotating Machinery*, Maui, Hawaii, May 8–11, 1994.
- [2] Y. Fukui, *JSME Int. J. Ser. III* 34 (1991) 144–148.
- [3] K.-L. Choy, E. Felix, *Mater. Sci. Eng. A* 278 (2000) 162–169.
- [4] K.A. Khor, Y.W. Gu, *Mater. Sci. Eng. A* 277 (2000) 64–76.
- [5] A. Lambros, A. Narayanaswamy, M.H. Santare, G. Anlas, *J. Eng. Mater. Technol.* 121 (1999) 488–493.
- [6] E. Braval, K. Aghahanian, S.J. Luszcz, *J. Am. Ceram. Soc.* 73 (1990) 2610–2614.
- [7] E. Manor, H. Ni, C.G. Levi, R. Mehrabian, *J. Am. Ceram. Soc.* 26 (1993) 1777–1787.
- [8] T. Belytschko, Y.Y. Lu, L. Gu, *Int. J. Numer. Meth. Eng.* 37 (1994) 229–256.
- [9] W.K. Liu, S. Jun, Y. Zhang, *Int. J. Numer. Meth. Fluids* 20 (1995) 1081–1106.
- [10] C.A. Duarte, J.T. Oden, *Comput. Meth. Appl. Mech. Eng.* 139 (1996) 237–262.
- [11] I. Babuska, J. Melenk, *Int. J. Numer. Meth. Eng.* 40 (1997) 727–758.
- [12] S.N. Atluri, T. Zhu, *Comput. Mech.* 22 (1998) 117–127.
- [13] S.N. Atluri, S. Shen, *The Meshless Local Petrov–Galerkin (MLPG) Method*, Tech Science Press, 2002.
- [14] R.A. Gingold, J.J. Monaghan, *Mon. Not. Roy Astron. Soc.* 181 (1977) 375–389.
- [15] J.K. Chen, J.E. Beraun, T.C. Carney, *Int. J. Numer. Meth. Eng.* 46 (1999) 231–252.
- [16] G.M. Zhang, R.C. Batra, *Comput. Mech.* 34 (2004) 137–146.
- [17] R.L. Hardy, *J. Geophys. Res.* 76 (1971) 1905–1915.
- [18] E.J. Kansa, *Comput. Math. Appl.* 19 (1990) 127–161.
- [19] M.A. Golberg, C.S. Chen, S.R. Karur, *Eng. Anal. Bound. Elem.* 18 (1996) 9–17.
- [20] G.E. Fasshauer, Solving partial differential equations by collocation with radial basis functions, in: A Le Méhauté, C. Rabut, L.L. Schumaker (Eds.), *Surface Fitting and Multiresolution Methods*, Vanderbilt University Press, Nashville, TN, 1997, pp. 131–138.
- [21] H. Wendland, *Math. Comput.* 68 (1999) 1521–1531.
- [22] G.R. Liu, Y.T. Gu, *J. Sound Vib.* 246 (2001) 29–46.
- [23] J.G. Wang, G.R. Liu, *Comput. Meth. Appl. Mech. Eng.* 191 (2002) 2611–2630.
- [24] J.R. Xiao, M.A. McCarthy, *Comput. Mech.* 31 (2003) 301–315.
- [25] J.R. Xiao, B.A. Gama, J.W. Gillespie Jr., E.J. Kansa, *Eng. Anal. Bound. Elem.* 29 (2005) 95–106.
- [26] J.R. Xiao, R.C. Batra, D.F. Gilhooley, J.W. Gillespie Jr., M.A. McCarthy, *Comput. Meth. Appl. Mech. Eng.* 196 (2006) 979–987.
- [27] J.R. Xiao, D.F. Gilhooley, R.C. Batra, J.W. Gillespie Jr., M.A. McCarthy, *Composites B*, in press.
- [28] H.K. Ching, S.C. Yen, *Composites B* 36 (2005) 223–240.
- [29] H.K. Ching, S.C. Yen, *Compos. Struct.* 73 (2006) 381–393.
- [30] J. Sladek, V. Sladek, Ch. Zhang, *Eng. Anal. Bound. Elem.* 29 (2005) 597–609.
- [31] J. Sladek, V. Sladek, Ch. Zhang, *Comput. Mater. Sci.* 28 (2003) 494–504.
- [32] J. Sladek, V. Sladek, J. Krivacek, Ch. Zhang, *Comput. Mech.* 32 (2003) 169–176.
- [33] B.N. Rao, S. Rahman, *Eng. Fract. Mech.* 70 (2003) 1–27.
- [34] A.J. Goupee, S.S. Vel, *Comput. Meth. Appl. Mech. Eng.* 195 (2006) 5926–5948.

- [35] L.F. Qian, R.C. Batra, L.M. Chen, *Composites B* 35 (2004) 685–697.
- [36] L.F. Qian, R.C. Batra, *J. Sound Vib.* 280 (2005) 415–424.
- [37] L.F. Qian, R.C. Batra, *J. Thermal Stresses* 27 (2004) 705–740.
- [38] L.F. Qian, R.C. Batra, *Comput. Mech.* 35 (2005) 214–226.
- [39] R.C. Batra, S. Vidoli, *AIAA J.* 40 (2002) 91–104.
- [40] D.F. Gilhooley, R.C. Batra, J.R. Xiao, M.A. McCarthy, J.W. Gillespie Jr., *Compos. Struct.* 80 (2007) 539–552.
- [41] A.J.M. Ferreira, R.C. Batra, C.M.C. Roque, L.F. Qian, P.A.L.S. Martins, *Compos. Struct.* 69 (2005) 449–457.
- [42] A.J.M. Ferreira, R.C. Batra, C.M.C. Roque, L.F. Qian, R.M.N. Jorge, *Compos. Struct.* 75 (2006) 593–600.
- [43] K.Y. Dai, G.R. Liu, K.M. Lim, X. Han, S.Y. Du, *Comput. Mech.* 34 (2004) 213–223.
- [44] S.S. Vel, R.C. Batra, *AIAA J.* 40 (2002) 1421–1433.
- [45] S.S. Vel, R.C. Batra, *J. Sound Vib.* 272 (2004) 703–730.
- [46] Z.Q. Cheng, R.C. Batra, *Composites B* 31 (2000) 97–106.
- [47] C.O. Horgan, A.M. Chan, *J. Elasticity* 55 (1999) 43–59.
- [48] R.C. Batra, *Elements of Continuum Mechanics*, AIAA, Reston, VA, USA, 2005.
- [49] J.G. Wang, G.R. Liu, *Int. J. Numer. Meth. Eng.* 54 (2002) 1623–1648.
- [50] L.F. Qian, R.C. Batra, L.M. Chen, *CMES* 4 (2003) 161–176.
- [51] G.H. Paulino, Z.H. Jin, *J. Appl. Mech.* 68 (2001) 129–134.
- [52] H. Stehfest, *Commun. Assoc. Comput. Mach.* 13 (1970) 47–49.
- [53] A. Sutradhar, G.H. Paulino, L.J. Gray, *Eng. Anal. Bound. Elem.* 26 (2002) 119–132.
- [54] S.S. Vel, R.C. Batra, *Int. J. Solids Struct.* 40 (2003) 7181–7196.
- [55] T. Mori, K. Tanaka, *Acta Metall.* 21 (1973) 571–574.
- [56] R. Hill, *J. Mech. Phys. Solids* 13 (1965) 213–222.
- [57] J.H. Kim, G.H. Paulino, *J. Appl. Mech.* 69 (2002) 502–514.
- [58] R.C. Batra, *Int. J. Numer. Meth. Eng.* 15 (1980) 145–160.
- [59] R.C. Batra, B.M. Love, *J. Thermal Stresses* 27 (2004) 1101–1123.
- [60] R.C. Batra, B.M. Love, *Eng. Fract. Mech.* 72 (2005) 1954–1979.
- [61] G.M. Zhang, R.C. Batra, *J. Comput. Phys.* 222 (2007) 374–390.
- [62] R.C. Batra, T.S. Geng, *J. Intell. Mater. Struct.* 13 (2002) 249–367.